Liu, Yining; Al Mahmud, Shamsul Arefeen; Ha-Van, Nam; Jayathurathnage, Prasad; Kyyra, Jorma; Tretyakov, Sergei A.

Noncoherent Power Combining for Free-Positioning Wireless Power Transfer in Large Area

Published in:
IEEE Transactions on Industrial Electronics

DOI:
10.1109/TIE.2024.3374391

Published: 01/01/2024

Document Version
Publisher's PDF, also known as Version of record

This article has been accepted for inclusion in a future issue of this journal. Content is final as presented, with the exception of pagination.

Noncoherent Power Combining for Free-Positioning Wireless Power Transfer in Large Area

Yining Liu, *Student Member, IEEE*, Shamsul Arefeen Al Mahmud, Nam Ha-Van, *Member, IEEE*, Prasad Jayathurathnage, *Senior Member, IEEE*, Jorma Kyyrä, *Member, IEEE*, and Sergei A. Tretyakov, *Fellow, IEEE*

***Abstract*—In this article, we propose a new coil-energizing method for multitransmitter (Tx) wireless power transfer (WPT) systems that enable complete freedom of receiver (Rx) positioning in a large area. The principle is based on noncoherent power combining, where multiple Tx coils are supplied in a predefined pattern by mixing two slightly different frequencies and four different phase angles. The powers delivered from Tx coils at two frequencies are then combined incoherently at the Rx side, resulting in full positional and rotational freedom for the Rx charging. The power transfer blind spots in conventional WPT systems are completely eliminated with the proposed noncoherent power combining method due to its natural robustness against cancelations. The experimental setup shows constant dc–dc power transfer efficiency around 90% for arbitrary Rx movements without any further requirements on dynamic controls of Txs or Rxs other than the simplest activation/deactivation.**

***Index Terms*—Blind spots elimination, full charging freedom, large transmitting area, noncoherent power combining, wireless power transmission (WPT).**

I. Introduction

EFFICIENT and uninterrupted wireless power transfer (WPT) in a large area facilitates wireless charging for a wide range of applications encompassing consumer electronics [1], kitchen appliances [2], and automated robots [3]. For example, a WPT system employing multiple transmitters (Txs) can be integrated into a table or kitchen top to enable seamless charging of multiple consumer electronics devices and kitchen appliances. Compared with the solutions using a single large Tx coil [4] or supply rails [5], applications of multiple small Tx coils [6], [7] are more flexible and provide possibilities of charging multiple receivers (Rxs) at the same time. In a multi-Tx system, it is easier to avoid standby losses and unwanted electromagnetic exposure by turning OFF the Tx coils in the uncoupled areas [8], [9]. However, due to the low misalignment tolerance of spiral coils, the power transfer encounters high pulsation since the magnetic field is weak at those positions between segmented coils. Comprehensive optimization of coil dimensions [10], [11] is required to mitigate coupling fluctuations for 1-D linear movements. For a larger charging area, overlapped coils [12] or dynamic controls [13] are needed to reduce the fluctuations in power and efficiency.

There have been numerous studies focusing on novel coil structures, e.g., double-D (DD) type, double-D-quadrature (DDQ) type, quadrature coils, flux-pipe, or crossed-flat solenoid coils [14], [15], [16], [17], [18] have been employed to optimize the transfer power and efficiency at misaligned Tx-Rx positions. In spite of the enhanced coupling coefficients, all these coupler structures work with the polarized flux in one single horizontal direction [14]. Nevertheless, the above coil designs still provide insights into building a large-area WPT system in terms of linear movement charging freedom. However, from the perspective of multi-Tx systems, apart from the misalignment tolerance, other considerations, e.g., cross-couplings between Tx coils [19], [20], [21] and magnetic leakage [22], also necessitate detailed analysis before tiling segmented Tx blocks to a transmitting area. In [20], a naturally decoupled Tx array was built with alternately placed DD and Q coils, where Rx having stacked DD and Q coils can pick up the power along the array. Staying with the existing solutions of tiled spiral Txs, Kim et al. [23] proposed a planar Rx structure with two subcoils, but individual rectifiers are necessary for each subcoil to realize omnidirectional WPT. Moreover, although the coupling coefficients between Tx and Rx have been greatly enhanced with the development of coil structures, blind spots (i.e., positions where the Rx obtains zero power) still exist in multi-Tx systems, because at some points the electromotive forces induced by several Txs cancel out each other at the Rx side. For instance, the duty cycle of the Tx supply

Manuscript received 28 October 2023; revised 27 January 2024; accepted 19 February 2024. This work was supported by Business Finland Research-to-Business under Grant 211964. *(Corresponding author: Yining Liu.)*

Yining Liu, Shamsul Arefeen Al Mahmud, Nam Ha-Van, Jorma Kyyrä, and Sergei A. Tretyakov are with the School of Electrical Engineering, Aalto University, 00076 Espoo, Finland (e-mail: yining.1.liu@aalto.fi; shamsul.almahmud@aalto.fi; nam.havan@aalto.fi; jorma.kyyra@aalto.fi; sergei.tretyakov@aalto.fi).

Prasad Jayathurathnage is with the School of Electrical Engineering, Aalto University, 00076 Espoo, Finland, and also with the Danfoss Drives, 33560 Tampere, Finland (e-mail: prasadku001@e.ntu.edu.sg).

Color versions of one or more figures in this article are available at https://doi.org/10.1109/TIE.2024.3374391.

Digital Object Identifier 10.1109/TIE.2024.3374391

TABLE I
COMPARISON BETWEEN LARGE-AREA WPT SYSTEMS USING CONVENTIONAL SOLUTIONS AND THE PROPOSED COIL-ENERGIZING METHOD

	References		[30]	[10]	[11]	[28], [29]	[5]	[3]	**Proposed**
Coil design	Tx structure		spiral	spiral	DD	long spiral + aux	interleaved meander	spiral	**spiral**
	Rx structure		spiral	spiral	DD	spiral + aux†	spiral	flux-pipe	**flux-pipe**
	Unlimited coil design freedom		✓	×	×	×	✓	✓	**✓**
Operation requirement	Number of frequencies		2	1	1	1	2	1	**2**
	Number of phases		1	1	1	1	2	2	**4**
	Rx detection and Tx control		position A/D*	position A/D	position A/D	position A/D	not needed amplitude modulation	position + orientation dynamic phase control	**position A/D**
Performance	charging freedom	single Rx	isolated spots	linear 1D + rotation	linear 1D	linear 1D	linear 2D + rotation	linear 2D + rotation	**linear 2D + rotation**
		multiple Rxs						linear 2D + rotation with blind spots	
	no flux leakage in uncoupled area		✓	✓	✓	×	×	✓	**✓**

* A/D refers to activation / deactivation. † aux is short for auxiliary.

voltage is adjusted in [24] to enhance the power transfer at weak coupling positions, but the control algorithm still cannot help with power transfer at blind spots because the total coupling at these positions is exactly zero.

Seeking other directions to reach full charging freedom by avoiding power cancelations, a few studies suggested applying dynamic control to Tx supplies based on instantaneous Rx position and orientation. To achieve full charging freedom, including linear and rotational movements in any desired direction, Al Mahmud et al. [3] proposed Rx detection and Tx activation methods based on input current sensing of each Tx in the system. To realize that, substantial sensing and control resources are imperative, particularly for accurate and fast detection of Rx orientation to activate necessary Tx coils and assign correct phases accordingly. Centralized control and communications among all the Txs are mandatory in such WPT systems due to the need for phase synchronization. These requirements bring a rapid increase in complexities to both control algorithms and system implementations compared with those systems that only need simple activation/deactivation that can be realized by modular ON/OFF control inside each Tx block [25] or passive circuits based on self-inductance variation [26] or impedance reflection [27]. In addition, systems with dynamic phase control do not offer any capacity for simultaneous charging of multiple devices, as it merely relocates blind spots from the Rx's current position to another location rather than completely eliminate them. On the other hand, the authors in [28] and [29] seek solutions to avoid power cancelation by designing unipolar coupler structures with auxiliary coils. However, the Tx coil structures are asymmetric, and only 1-D charging freedom is discussed for these designs. Besides, development in structure complexity brings more efforts to the design process regarding tradeoffs between more parameters and the non-negligible increase in coil parasitics, possible issues of magnetic leakage also require further analysis. Based on the discussions above, Table I presents a comparison between the existing solutions and the proposed method for realization of large-area WPT.

Dealing with these problems of complicated coil designs and control/detection algorithms, in this article, we propose a new coil-energizing pattern based on the noncoherent method that combines power at multiple frequencies. The proposed approach enables wireless charging free from any blind spots and eliminates the need for complex control mechanisms. We introduce a prefixed energizing pattern for multiple Txs with the smallest repetitive unit of 4 × 4 blocks, mixing two slightly different operating frequencies and four phase angles. The arbitrary-sized Tx area energized by the proposed pattern grants complete positional and rotational charging freedom for multiple Rxs. The proposed pattern works in line with the existing multi-Tx WPT system structures with simple detection and activation methods.

The rest of this article is organized as follows. In Section II, we introduce the proposed multi-Tx configuration and corresponding coil-energizing method. The noncoherent power combining at Rx side including two special cases are analyzed in detail in Section III. Section IV presents the experimental prototype and measurement results. Finally, Section V concludes this article.

II. PROPOSED COIL-ENERGIZING METHOD FOR MULTI-TX WPT SYSTEMS

A. Proposed Coil-Energizing Configuration

Fig. 1 presents the proposed coil-energizing method of multiple Txs in a large-area WPT system. A Tx block formed by a spiral Tx coil connected to a compensation circuit is shown in Fig. 1(a). In each block, we mix input currents at two slightly different frequencies by supplying two block terminals Tx$_{ij}$a and Tx$_{ij}$b with input voltages at frequencies f_1 and f_2, respectively. The phase angles of these two voltage components, $p_{ij,1}$ and $p_{ij,2}$, are selected from 0°, 90°, 180°, and 270°. Inputs at these two frequencies are marked by yellow (f_1) and blue (f_2) colors in Fig. 1(a) and (c), with the corresponding phase angles written on top. The physical layout of a multi-Tx area is illustrated in Fig. 1(b), tiled by identical spiral coils. A Tx coil is numbered as Tx$_{ij}$ following its position in the ith row and jth column.

In Fig. 1(c), we illustrate the proposed energizing pattern for the given multi-Tx area in terms of phase relations at each frequency. The phases at each frequency are varied periodically every four blocks along both x and y directions. Therefore, the smallest repetitive unit of this free-positioning pattern is a 4 × 4 cluster (e.g., the area surrounded by the black border) with the

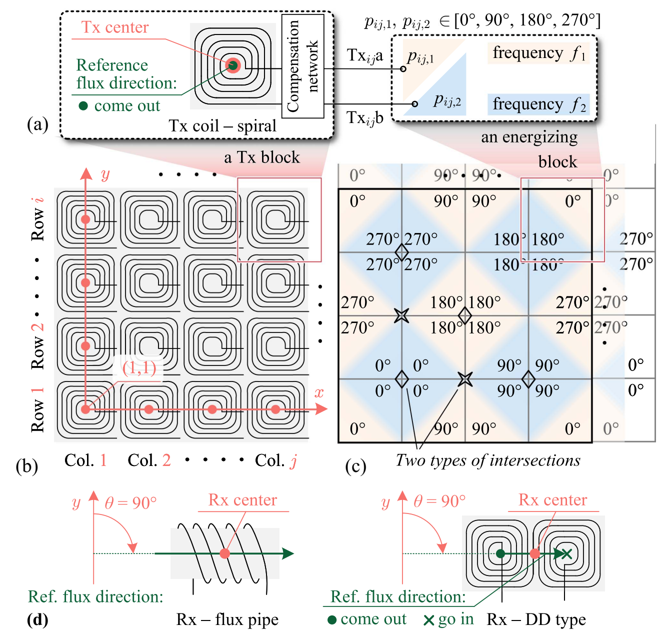

Fig. 1. Proposed coil-energizing method for multi-Tx WPT systems (top view). (a) Tx block: the coil structure and connections. (b) Physical layout of multiple Tx coils in a large area. Each coil Tx_{ij} is labeled by its location at row i, column j. An xy coordinate system is defined to describe Rx movements, with the x, y axis directions following j, i increments. The coordinate origin (1,1) is at the center of Tx_{11}. Coordinates x, y indicate the location of the Rx center, and their values are equal to the actual distance (in cm) normalized to the Tx coil size (in cm). (c) Proposed Tx-area energizing pattern [one energizing block indicates the supply frequencies and phases connected to a- and b-terminals of the corresponding Tx block, cf., (a)]. (d) Valid Rx coil structures. The Rx orientation is defined by angle θ, i.e., the clockwise-measured angle of the Rx reference flux direction from the positive y-direction.

combinations of two frequencies and four phase values. However, it is noted that the proposed pattern can always provide full Rx-charging freedom for any size of the charging area with an arbitrary number of Tx blocks, i.e., the free-positioning feature is not limited to the implementations with integer multiples of 4×4 clusters, areas with either fewer or more Tx blocks still provide full charging freedom as long as the proposed energizing pattern is followed. More specifically, there are in total two typical intersections appearing alternately inside the pattern, cf., Fig. 4(b) and (a), respectively, given in the following.

1) *Intersection* ♢*:* Four surrounding Tx blocks are energized with the same phase at one frequency (either f_1 or f_2), and four different phases (varying with 90° gap in clockwise or counterclockwise direction) at the other frequency.
2) *Intersection* ✧*:* Four surrounding Tx blocks are energized by two phases (with 90° gap) at each frequency. Blocks in the same column are in-phase in f_1 (or f_2), and blocks in the same row are in-phase at the other frequency.

These two types of intersections are classified based on two different types of power combinations, which will be discussed in detail in Section III-A.

The proposed Tx-energizing method easily works in line with existing WPT system structures. In terms of robust power transfer against misalignments, Rxs based on either DD or flux-pipe structures are compatible with such multi-Tx WPT systems.

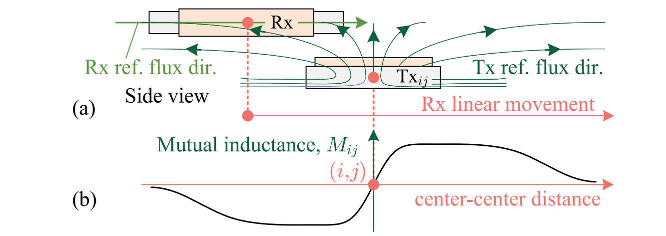

Fig. 2. (a) Illustration of Rx movements with regard to the Tx_{ij} coil, with the defined reference flux direction for each coil. (b) Mutual inductance M_{ij} variations in terms of the value and sign (positive/negative).

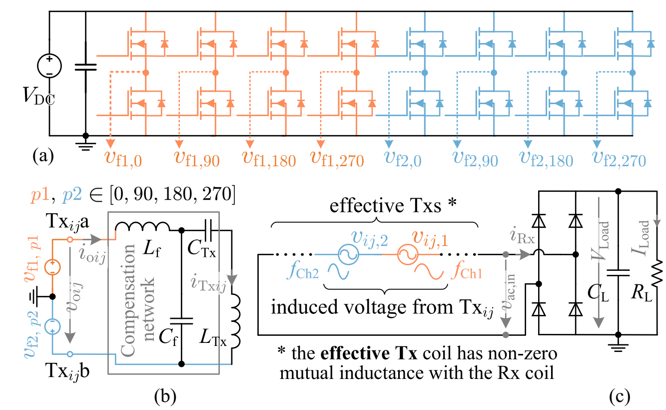

Fig. 3. (a) N-legged converter is used to provide the required ac voltage (corresponding frequencies and phases are shown for $N=8$) to supply the Tx blocks. (b) Equivalent circuit for a Tx building block [cf., Fig. 1(c)], indicating the connections of the *LCC* compensation network and terminals Tx_{ij}a (connects to the f_1 branch) and Tx_{ij}b (connects to the f_2 branch). (c) Rx-side simplified circuit with ideal ac voltage sources. The induced voltage from each Tx coil contains both frequencies f_1 and f_2, and all the effective Txs with nonzero mutual inductance with the Rx will provide induced voltage at the Rx side.

Based on the reference flux directions inside the Rxs [defined in Fig. 1(d)] and in the identical Txs [defined in Fig. 1(a)], the Rx has a positive mutual inductance M_{ij} with the coil Tx_{ij} when its flux flows through the Rx in the same direction as the Rx reference direction, cf., Fig. 2(a) on the right-hand side, while M_{ij} is negative when the flux directions are opposite to each other, cf., Fig. 2(a) on the left-hand side.

B. Realization of the AC Supply At the Tx Side

To realize the energizing pattern proposed in Section II-A, the N-legged converter topology can be used [31]. There are in total eight legs in Fig. 3(a), providing all the combinations of supply frequencies (f_1, f_2) and phases (0°, 90°, 180°, 270°). Considering only the dc and fundamental components, the voltage signal $v_{\mathrm{f}n,pn}$ at the middle switching node of one converter leg can be written as

$$v_{\mathrm{f}n,pn}(t) = \frac{V_{\mathrm{dc}}}{2} + \frac{2V_{\mathrm{dc}}}{\pi} \sin\left(\omega_n t - p_n\right) \quad (1)$$

where $n = 1, 2$ indicates the frequency f_1 or f_2 (angular frequencies $\omega_{1,2}$), and this notation of n is used also in the following. $p_n \in [0°, 90°, 180°, 270°]$ is the phase value for the corresponding frequency channel.

As illustrated in Fig. 1(a), we inject two frequencies to one Tx block by connecting its terminals, Tx$_{ij}$a and Tx$_{ij}$b, to the middle switching nodes of the corresponding converter legs $v_{\mathrm{f}1,p1}$ and $v_{\mathrm{f}2,p2}$. Due to linearity of the coils, the circuit can be separately analyzed at each frequency, and the total voltage or current in time domain can be obtained simply by adding up the components at the two frequencies. In our case, the input ac voltage at each frequency is

$$v_{\mathrm{o}ij,n}(t) = V_{\mathrm{o}} \sin(\omega_n t - p_{ij,n}), \quad V_{\mathrm{o}} = 2V_{\mathrm{dc}}/\pi \tag{2}$$

where $p_{ij,n} \in [0°, 90°, 180°, 270°]$ is the phase p_n of the corresponding leg connected to the block terminal Tx$_{ij}$a or Tx$_{ij}$b. As it is obvious from Fig. 3(b), the total voltage reads

$$v_{\mathrm{o}ij}(t) = v_{\mathrm{f}1,p1}(t) - v_{\mathrm{f}2,p2}(t) = \sum_{n=1,2} v_{\mathrm{o}ij,n}(t). \tag{3}$$

Similarly, the currents in Tx block are mixtures of both frequencies f_1 and f_2. By applying Kirchhoff's law, the input current of the *LCC* compensation circuit [10] $(L_{\mathrm{f}}, C_{\mathrm{f}}, C_{\mathrm{Tx}})$ is derived as

$$\vec{i}_{\mathrm{o}ij} = \sum_{n=1,2} \frac{M_{ij}^2}{L_{\mathrm{f}}{}^2} \frac{\vec{v}_{\mathrm{o}ij,n}}{(\pi^2/8)R_{\mathrm{L}}} \tag{4}$$

where $\vec{v}_{\mathrm{o}ij,n}$ represents the phasor form of the ac supply voltage in (2). Having the system dc load resistance R_{L} in (4), the current $\vec{i}_{\mathrm{o}ij}$ from the inverter output is shaped by the load-side operations. In contrast, the current flowing through Tx coil L_{Tx} is given as

$$\vec{i}_{\mathrm{Tx}ij} = \sum_{n=1,2} -\mathrm{j}\,\frac{\vec{v}_{\mathrm{o}ij,n}}{\omega_n L_{\mathrm{f}}} \tag{5}$$

determined by the supply voltage components $v_{\mathrm{o}ij,1}$ and $v_{\mathrm{o}ij,2}$, the Tx current also contains both frequencies and is independent of load or mutual inductance variations. Therefore, the *LCC* compensation circuit provides load-independent current through the Tx coil, which ensures safe operation of the WPT system for those Tx coils with no coupling to the Rx [32].

In the proposed method, the Tx supply pattern is fixed and does not require any phase or current control. However, to achieve even better performance in terms of higher system efficiency and minimized electromagnetic exposure, a dynamic activation method can also be applied to the Tx area based on any existing Rx detection methods, e.g., the detection and activation method in [3].

III. Power Combining at the Rx Side

In this section, we discuss how the WPT channel is established with the proposed energizing pattern. Considering one WPT channel, i.e., from one Tx coil to one Rx at one single frequency, the Tx-side circuit can be modeled as an induced voltage source in the Rx-side equivalent circuit. The phase and amplitude of the induced voltage source are determined by the mutual inductance as well as the source voltage [33], according to the time-domain equation

$$v_{ij,n}(x, y, \theta, t) = -\frac{M_{ij}(x, y, \theta)}{L_{\mathrm{f}}} V_{\mathrm{o}} \cdot \sin(\omega_n t - p_{ij,n}) \tag{6}$$

where (x, y, θ) describes the Rx position and orientation, and $M_{ij}(x, y, \theta)$ is the mutual inductance between Rx and a specific Tx, Tx$_{ij}$. Therefore, any effective Tx coil that has nonzero mutual inductance with the Rx (i.e., $M_{ij}(x, y, \theta) \neq 0$) contributes two induced voltage sources $v_{ij,1 \text{ and } 2}$ (representing two frequencies) at Rx side, as depicted in Fig. 3(c).

Following (6), since the induced voltage is always load independent, the Rx-side power combining is also represented by combining of the induced voltage sources. The total induced voltage of the Rx circuit, $v_{\mathrm{ac,in}}$, is the sum of the induced voltage components from all the effective Tx coils at both frequencies, given as

$$\begin{aligned} v_{\mathrm{ac,in}}(x, y, \theta, t) &= \sum_{ij \in M_{ij}(x,y,\theta) \neq 0} v_{ij,1}(x, y, \theta, t) \\ &\quad + \sum_{ij \in M_{ij}(x,y,\theta) \neq 0} v_{ij,2}(x, y, \theta, t) \\ &= v_{\mathrm{in},1}(x, y, \theta, t) \;+\; v_{\mathrm{in},2}(x, y, \theta, t) \end{aligned} \tag{7}$$

where $v_{\mathrm{in},n}$ ($n = 1$ or 2) is the sum of all the induced voltage components at the same frequency f_n, represented by their amplitudes $A_{\mathrm{in},n}$ and phases $p_{\mathrm{in},n}$ as

$$v_{\mathrm{in},n}(x, y, \theta, t) = A_{\mathrm{in},n}(x, y, \theta) \sin[\omega_n t - p_{\mathrm{in},n}(x, y, \theta)]. \tag{8}$$

Here, we consider amplitudes as unsigned values. Therefore, the negative sign in (6) and the signs of $M_{ij}(x, y, \theta)$ (cf., Fig. 2) are all included to the induced voltage phase $p_{\mathrm{in},n}$.

A. Noncoherent Power Combining of Inputs at Multiple Frequencies

Applying the power combining (7) for a given Rx position (x, y, θ), when nonzero voltage components at more than one frequency appear on the Rx side, i.e.,

$$A_{\mathrm{in},1}(x, y, \theta) \neq 0 \;\cup\; A_{\mathrm{in},2}(x, y, \theta) \neq 0 \tag{9}$$

the power is combined in a noncoherent manner.

Based on the definition in (9), noncoherent power combining happens at most of the Rx positions within the Tx area. If we take position $(x, y, \theta) = (2.5, 1.5, 45°)$ as an example, given in Fig. 4(a), by considering f_1 and f_2 separately, the induced voltage at the same frequency can be first added up following their phasor relations. Thus, we obtain the total induced voltage $\vec{v}_{\mathrm{in},1}$ for frequency f_1, and $\vec{v}_{\mathrm{in},2}$ for frequency f_2, cf., (7) for their time-domain forms.

Furthermore, $v_{\mathrm{in},1}$ and $v_{\mathrm{in},2}$ at two different frequencies are combined to $v_{\mathrm{ac,in}}$ in a noncoherent way, where the rules of phasor combining are not applicable. As shown in Fig. 4(a2), the relative phase difference between $\vec{v}_{\mathrm{in},1}$ and $\vec{v}_{\mathrm{in},2}$ varies with time since their frequencies are not equal, leading to a time-varying amplitude of the total induced voltage $\vec{v}_{\mathrm{ac,in}}$. To add up voltage components at different frequencies, we consider the

This article has been accepted for inclusion in a future issue of this journal. Content is final as presented, with the exception of pagination.

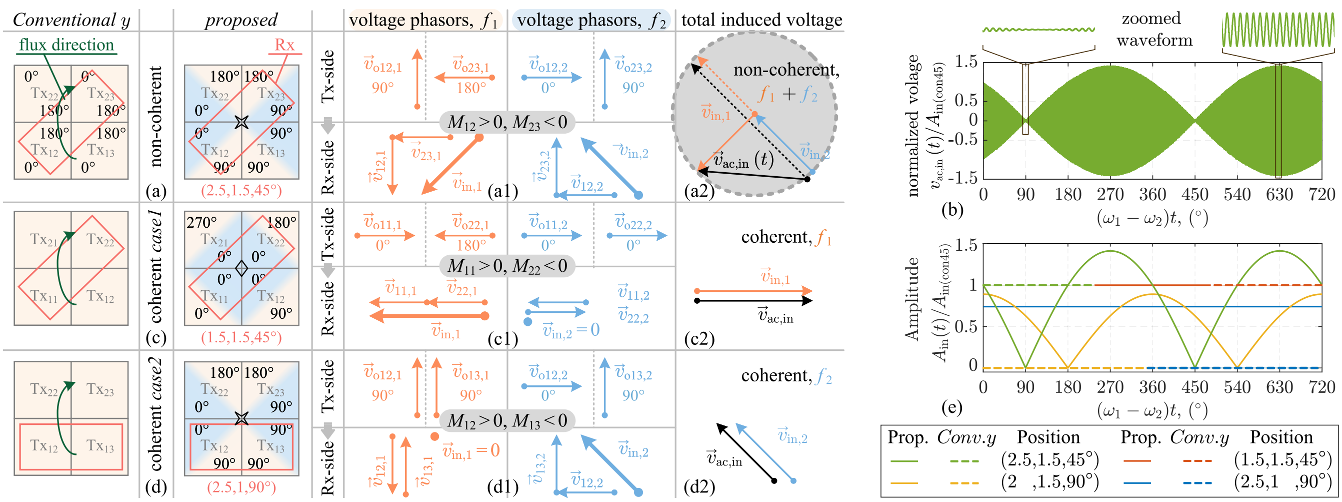

Fig. 4. Examples of Rx-side power combining (induced voltage phasors) within the Tx area: (a) noncoherent combining with multiple frequencies, (c) coherent, special *Case 1:* single frequency in same phase, and (d) coherent, special *Case 2:* single frequency with 90° phase difference, and total induced voltage: (b) $v_{\mathrm{ac,in}}$ instantaneous waveform in noncoherent combining and (e) time-varying amplitude A_{in} at four example positions.

time-domain equation

$$\begin{aligned} v_{\mathrm{ac,in}}(x,y,\theta,t) &= \sum_{n=1,2} A_{\mathrm{in},n}(x,y,\theta)\sin(\omega_n t - p_{\mathrm{in},n}) \\ &= A_{\mathrm{in}}(x,y,\theta,t)\sin\left[\frac{\omega_1+\omega_2}{2}t + \phi_{\mathrm{in}}(x,y,\theta,t)\right] \end{aligned} \tag{10}$$

where amplitude A_{in} and phase ϕ_{in} of the total induced voltage $v_{\mathrm{ac,in}}$ are calculated as (11) and (12) is shown at the bottom of this page. These equations indicate that with noncoherent combining, the amplitude and phase of the total induced voltage are also functions of time instead of only affected by the Rx position. Such features are greatly important in terms of eliminating blind spots that exist in conventional systems where only coherent power combining takes place.

For example, at the position in Fig. 4(a), time-domain waveform $v_{\mathrm{ac,in}}(2.5, 1.5, 45°, t)$ is plotted in Fig. 4(b), its amplitude $A_{\mathrm{in}}(t)$ varies with time in a period $T_s = 1/|f_1 - f_2|$. The waveform $A_{\mathrm{in}}(2.5, 1.5, 45°, t)$ is given in Fig. 4(e). Rx position $(x, y, \theta) = (2, 1.5, 90°)$ is a blind spot to the *Conventional* y pattern, but power can still be combined incoherently in the *proposed* WPT system. $A_{\mathrm{in}}(2, 1.5, 90°, t)$ waveform for the *Conventional* y and the *proposed* Tx areas are drawn as dashed and solid yellow lines in Fig. 4(e), respectively. The $A_{\mathrm{in}}(t)$ waveforms from noncoherent combining show only instantaneous moments of zero power transfer, with a recurring period of T_s. Therefore, at conventional blind spot positions, the time-averaged root-mean-square (rms) amplitude of the noncoherently combined induced voltage source is $A_{\mathrm{in(rms)}} = (A_{\mathrm{in},1} + A_{\mathrm{in},2})/2$, in comparison with $A_{\mathrm{in(rms)}} \equiv 0$ in the conventional coherently combined case.

B. Special Positions: Coherent Power Combining at a Single Frequency

When examining power combining across the entire Tx area, specific positions exist where the induced voltage components at one frequency incidentally nullify each other. In two examples given in Fig. 4(c) and (d), one of the voltage components $v_{\mathrm{in},1}$ or $v_{\mathrm{in},2}$ is nullified. Therefore, the total induced voltage $v_{\mathrm{ac,in}}$ contains one single frequency in such special cases, its rms value is calculated as $A_{\mathrm{in(rms)}} = A_{\mathrm{in},n}/\sqrt{2}$, where $A_{\mathrm{in},n} \neq 0$. We will explain these two types of special power combining cases individually in the following.

1) Case 1: Coherent Power Combining With the Same Phase, e.g., Fig. 4(c): At position $(x, y, \theta) = (1.5, 1.5, 45°)$, two effective Tx coils, Tx_{11} and Tx_{22}, have the same mutual inductances with the Rx, but of the opposite signs. From (6) we observe that the phase of induced voltage is decided jointly by the phase of Tx-block supply $\vec{v}_{oij,n}$ and the sign of mutual inductance M_{ij}. Due to the 180° phase shift between supplies $\vec{v}_{o11,1}$ and $\vec{v}_{o22,1}$, their f_1-frequency induced voltage components, $\vec{v}_{11,1}$ and $\vec{v}_{22,1}$, have the same phases and are added up on the Rx side. In contrast, since the f_2-frequency components of Tx_{11} and Tx_{22} supply voltages are in-phase, their induced voltage components $\vec{v}_{11,2} = -\vec{v}_{22,2}$ cancel out with each other and do not contribute to the power transfer. The corresponding phasor relations at two frequencies are also illustrated in Fig. 4(c1).

$$A_{\mathrm{in}}(x,y,\theta,t) = \sqrt{A_{\mathrm{in},1}^2(x,y,\theta) + A_{\mathrm{in},2}^2(x,y,\theta) + 2A_{\mathrm{in},1}A_{\mathrm{in},2}\cos\{(\omega_1-\omega_2)t + [p_{\mathrm{in},1}(x,y,\theta) - p_{\mathrm{in},2}(x,y,\theta)]\}} \tag{11}$$

$$\phi_{\mathrm{in}}(x,y,\theta,t) = \arctan\left\{\frac{A_{\mathrm{in},1}(x,y,\theta) - A_{\mathrm{in},2}(x,y,\theta)}{A_{\mathrm{in}1}(x,y,\theta) + A_{\mathrm{in},2}(x,y,\theta)}\tan\left[\frac{\omega_1-\omega_2}{2}t + \frac{p_{\mathrm{in},1}(x,y,\theta) - p_{\mathrm{in},2}(x,y,\theta)}{2}\right]\right\}. \tag{12}$$

TABLE II
SYSTEM SPECIFICATIONS AND COIL PARAMETERS

parameter	value	param.	value	param.	value
f_1, f_2	$199, 201$ kHz	$V_{\rm DC}$	30 V	$R_{\rm L}$	$100\,\Omega$
Tx size*	$157 \times 157 \times 1.5$	$L_{\rm Tx}$	$21\,\mu$H	$C_{\rm Tx}$	67.2 nF
Rx size*	$255 \times 115 \times 1.5$	$L_{\rm Rx}$	$360\,\mu$H	$C_{\rm Rx}$	1.75 nF
Distance	35 mm	$L_{\rm f}$	$11.4\,\mu$H	$C_{\rm f}$	55.2 nF

* All the dimensions are for one coil: length × width × thickness, in (mm).

Therefore, the Rx encounters a coherent power combining at a single frequency f_1, with phasors added up in phase. As indicated in Fig. 4(c2), the total induced voltage $v_{\rm ac,in}$ contains only one frequency, so its amplitude is a constant value with regard to time. The amplitude $A_{\rm in}(1.5, 1.5, 45^\circ)$ is plotted as an orange solid line in Fig. 4(e), which gives the same result as the *Conventional* y setup, cf., dashed line in orange.

2) Case 2: Coherent Power Combining With 90° Phase Shift, e.g., Fig. 4(d): At $(x, y, \theta) = (2.5, 2, 90^\circ)$, *Case 2* corresponds to a similar coupling situation as *Case 1* where $M_{22} = -M_{23}$. The f_1 supply voltage for coils $\rm Tx_{22}$ and $\rm Tx_{23}$ are in-phase, i.e., $p_{22,1} = p_{23,1} = 180^\circ$, resulting in full cancelation of the Rx-side induced voltages, given $v_{22,1} + v_{23,1} = 0$. However, the f_2 supply voltages have a 90° phase difference in this special case instead of the 180° in *Case 1*, and the induced voltage phasors are orthogonal to each other, as shown in Fig. 4(d1). Compared with the power combining in *Case 1*, the total induced voltage has a lower amplitude due to the phase-shifted add up; however, the two induced voltage phasors still do not cancel each other. This is also the main reason for selecting the phase difference as 90°, since the induced voltage phasor in either 0° or 180° will never cancel even partially with the phasor at 90° or 270°. The induced voltage amplitude in special *Case 2* is also plotted in Fig. 4(e) for straightforward comparison with other power combining cases.

C. Selection of the Switching Frequencies f_1 and f_2

Specifications and coil parameters of the WPT system implementation are given in Table II. Operating frequencies around 200 kHz are selected as an example considering the *Qi* standards for middle-range WPT [34]. In terms of the tradeoff between the WPT link efficiency and the rectifier output dc filtering capacitance $C_{\rm L}$, cf., Fig. 3, too small frequency gap between f_1 and f_2 creates difficulties for filtering the output voltage ripple, whereas a large frequency gap will degrade the WPT link efficiency [33].

Therefore, we conduct simulations to select the appropriate combination of frequency gap and dc capacitance values. The ripple and rms values of the output voltage are given in Fig. 5 with regard to frequency gaps. The simulation is built based on the system parameters at Rx position (2.5,1.5,45°), where the noncoherent effect is fully revealed. In order to get rid of the high dc voltage ripple while still maintaining a high rms value, the 2-kHz frequency gap and a 90 μF dc filtering capacitor are selected for the proposed WPT system.

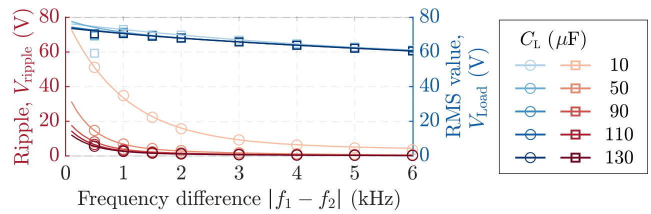

Fig. 5. DC load voltage ripple $V_{\rm ripple}$ and the rms value $V_{\rm Load}$ with regard to variations of frequency gap $|f_1 - f_2| \in [0.5, 6]$ kHz and dc output capacitance $C_{\rm L} \in [10, 130]\,\mu$F. $(f_1 + f_2)/2$ is kept at 200 kHz.

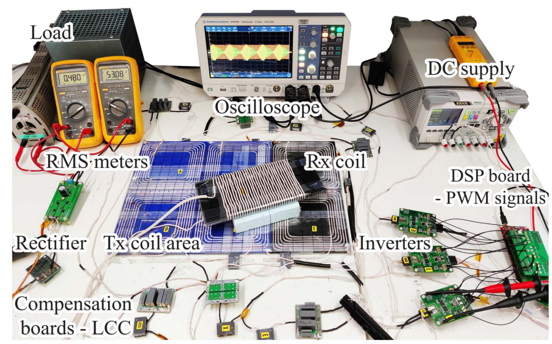

Fig. 6. Experimental setup of a WPT system with the proposed Tx coil-energizing method.

IV. EXPERIMENTAL VERIFICATION

A. Experimental Setup

Following the specifications in Table II, we built a laboratory prototype WPT system with spiral Tx coils and a flux-pipe Rx coil. The Tx area is energized following the pattern proposed in Fig. 1(a). Due to the symmetry of the proposed energizing pattern, as discussed in Sections II-A and III-A, the charging area is built as a scaled-down version with 3×2 blocks. Including both two typical types of *Intersections* ◇ *and* ✧, the presented area is able to show all the special Rx positions for different types of power combining. Following Section II-B, Tx coils equip *LCC* compensation circuits, and series compensation is used for Rx tuning, for implementation simplicity. Considering the variation in Tx self-inductance during Rx movement [26], each Tx coil is tuned with the Rx on top, similarly, Rx is tuned inside the Tx area. In addition, cross-coupling between the Tx coils is compensated using decoupling inductors, as proposed in [3]. Therefore, the Tx blocks act as independent and decoupled units. In summary, the compensation topology or the cross-coupling cancelation methods are not affected by the types of power combining.

Fig. 6 shows a photo of the experiment WPT system. The Tx blocks are driven by six half-bridge legs (model *LMG5200*) containing the required frequency and phase combinations, and a digital signal processor *TMS320F28379* is used to generate corresponding control signals. An *FSV10120 V*-based diode bridge rectifier is used at the Rx side, together with a passive resistor bank as the load. The waveforms are observed using an

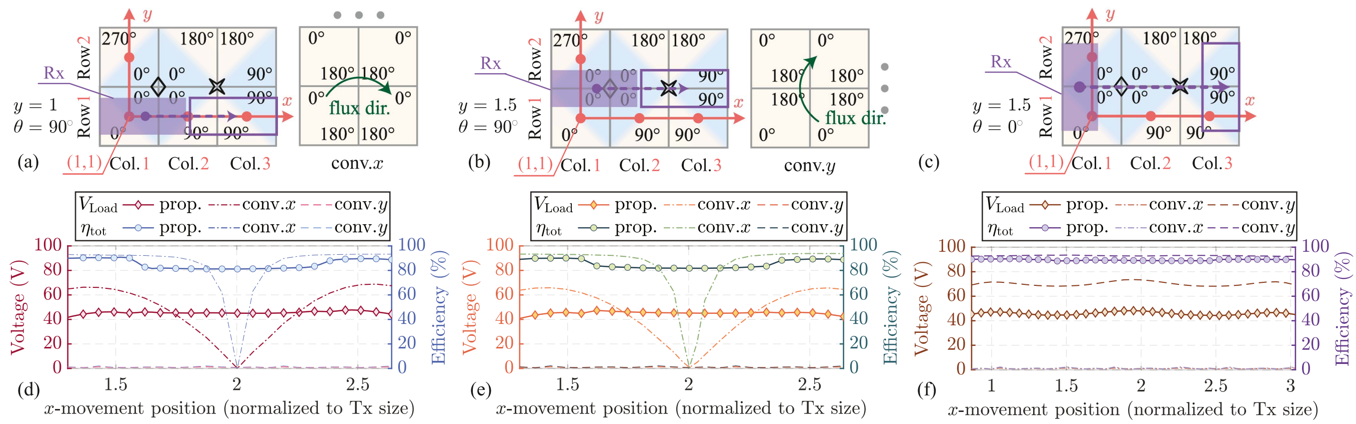

Fig. 7. Comparison between conventional and the proposed Tx-area energizing patterns in terms of the dc output voltage and dc–dc efficiency, with different *linear* Rx movements. (a) Rx device with $\theta = 90^\circ$ moving linearly in the x-direction, the Rx center is located in the middle of one row of the Tx area. (b) Rx device with $\theta = 90^\circ$ moving linearly in the x-direction between two adjacent rows of the Tx area. (c) Rx device with $\theta = 0^\circ$ moving linearly in the x-direction between two adjacent rows of the Tx area. (d)–(f) Measured dc output voltage V_{Load} and the dc–dc efficiency η_{tot} for three types of linear movements in (a)–(c), respectively. The definitions of (x, y, θ) follows Fig. 1.

oscilloscope, and dc voltages and currents are measured using industrial-grade true-RMS meters (*FLUKE 28-II*).

The prototype system works at 20–40 W power level, the power at a specific charging position can be calculated through the measured load voltage and the resistance given in Table II. Next, we analyze the experimental performance of the WPT system using the proposed energizing pattern. To this end, the load voltage and efficiency of the experimental prototype WPT system are presented against different Rx movements, and the results are compared with the conventional approaches.

B. Charging Freedom Against Rx Linear Movements in x- and y-Directions

First, the Rx coil is moved linearly in the x-direction while keeping the orientation of the Rx aligned with either x or y axis. Fig. 7(a)–(c) present three types of movements with different orientations θ. The measurements of output voltage and efficiency are given in Fig. 7(d)–(f), where x and y values are normalized to the Tx coil width, see the definitions in Fig. 1.

When the Rx coil moves along the x-direction with reference flux also in x-orientation [i.e., $\theta = 90^\circ$, cf., Fig. 7(a) and (b)], the proposed energizing pattern ensures an almost constant output voltage and efficiency by combining the power incoherently. Special *Case 2* happens at $x = 1.5, 2.5, \ldots$, where coherent power combining is realized with 90° phase shift. In comparison, the *Conventional* x supplying pattern exhibits blind spots with null output and efficiency when the center of the Rx coil is aligned with the center of one Tx coil, i.e., at $x = 1, 2, 3, \ldots$, since the adjacent two columns have the same flux directions and their induced voltage components cancel out at the Rx side. This cancelation never happens with our proposed supplying pattern as the Rx side obtains noncoherently combined power at this position. Moreover, the Rx could not receive any power with *Conventional* y pattern due to the zero total coupling.

When the Rx moves in the x-direction at $y = 1.5$ but oriented in $\theta = 0^\circ$, as shown in Fig. 7(c), both the *proposed* and the *Conventional* y patterns exhibit continuous power reception at Rx without any blind spots. Both approaches result in a similar system dc–dc efficiency around 90 %. The voltage amplitude in the proposed case is slightly lower than the *Conventional* y due to the 90° phase shift in coherent power combining, cf., Section III-B2. Nevertheless, the voltage can be easily restored by adjusting the supply voltage. However, with the *Conventional* x pattern, the flux provided by Txs always flows in the x-direction, which does not couple with the Rx, resulting in almost zero output voltage.

C. Charging Freedom for Rx Rotational Movements

Next, to demonstrate the robust performance against different angular orientations, we study the load voltage and efficiency within 0° to 180° rotation angles of the Rx device. The performance is the same for $\theta \in [180^\circ, 360^\circ]$ due to the symmetry of the Rx structure. The system performance against Rx rotation angles at two typical intersection positions, i.e., at *Intersection* ♢: (1.5, 1.5) and *Intersection* ✧: (2.5, 1.5), are shown in Fig. 8(a) and (b). In comparison, these two intersection positions are the same in *Conventional* x *or* y patterns in terms of power transfer, so the measurement curves of two conventional cases are split among Fig. 8(d) and (e) for better clarity. It can be seen that the proposed approach exhibits continuous power reception at all rotation angles, whereas both *conventional* x, y suffer from blind spots with zero power and efficiency. Due to the in-phase supplies in f_2, the Rx rotation at *Intersection* ♢: (1.5, 1.5) [cf., Fig. 8(d)] exhibits coherent power combining, varying between *Case 1* (the same phase) and *Case 2* (90°-shifted phase). At *Intersection* ✧: (2.5, 1.5) [cf., Fig. 8(e)], the power is mostly combined incoherently, and special *Case 2* only happens at the quadrant angles. Regardless of the power combining types, the proposed energizing pattern demonstrates power transfer with full Rx rotational freedom with constant dc–dc efficiency over 84 %. The variation among different types of power combining leads to small fluctuations in the output voltage, while its value

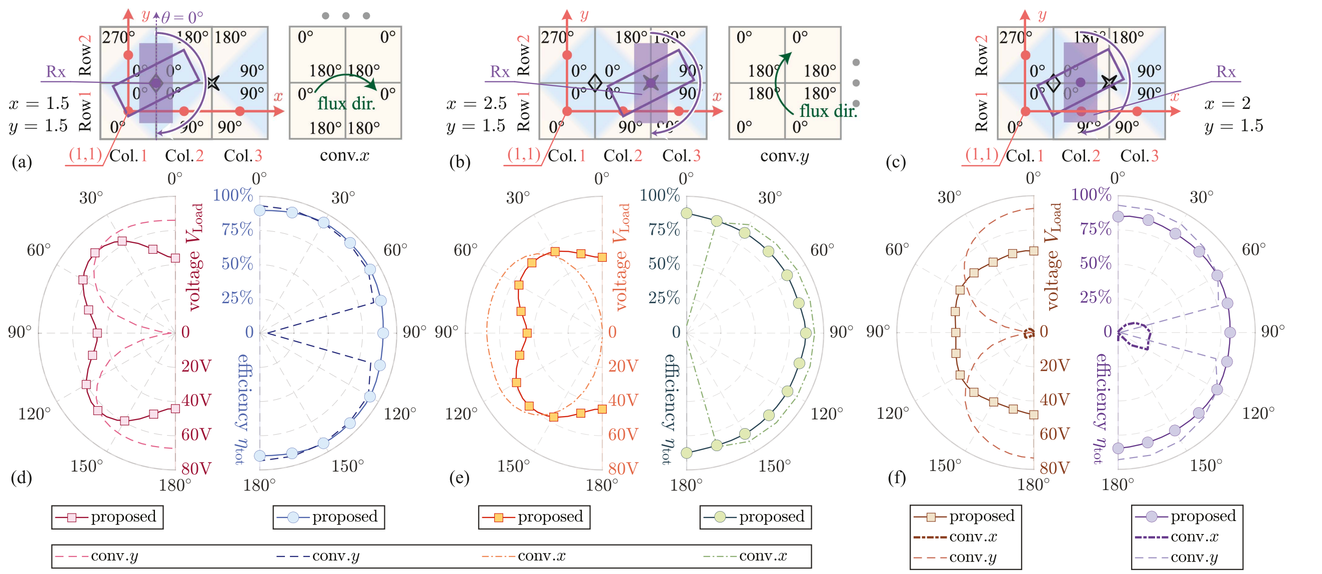

Fig. 8. Comparison between conventional and the proposed Tx-area energizing configurations in terms of the dc output voltage and the dc–dc efficiency, with different *rotational* Rx movements. 0°–180° rotation with Rx center positioned (a) at the *Intersection* ◊ when $(x, y) = (k+i, k+j)$, $k = 1.5, 2.5, \ldots$, $i, j \in (0, 2, 4, 6, \ldots)$, (b) at the *Intersection* ✧ when $(x, y) = (k, k \pm j)$, $k = 1.5, 2.5, \ldots$, $j \in (1, 3, 5, \ldots)$, $x > 1, y > 1$, and (c) at the edge between two rows or between two columns. (d)–(f) Measured dc output voltage V_{Load} and the dc–dc efficiency η_{tot} for three types of rotational movements in (a)–(c), respectively. $\theta = 0°$ when the Rx reference flux direction is in the positive y-direction, cf., Fig. 1.

can be easily adjusted using basic voltage regulation methods, e.g., [35], since the power is always transferred with good efficiency. In contrast, completely zero power transfer at *conventional* x, y blind spots (the quadrant Rx orientations) cannot be improved at all due to the null efficiency.

Finally, Fig. 8(f) shows the output voltage and efficiency when the Rx center is located in the middle of one Tx column, i.e., $(x, y) = (2, 1.5)$. The proposed method still provides continuous power transfer with almost constant efficiency, while *Conventional* y pattern shows blind spots when Rx orients along the x-direction, and there is completely no power transfer at any angle with *Conventional* x.

D. Experimental Waveforms and Loss Distribution

The experimental voltage/current waveforms of the Tx and Rx are shown in Figs. 9 and 10(a), respectively, for the noncoherent and coherent power combining cases. Rx position $(x, y, \theta) =$ (2.5,1.5,45°) in Fig. 4(a) is still used as the example for noncoherent combining illustration. According to the analysis in Section III-A, the noncoherent power transfer is time-varying, and due to the existence of a large dc filtering capacitance at the system output, the instantaneous power transfer is brought down to zero when it is not enough to supply the output, indicated by current i_{Rx} in Fig. 9(b). Therefore, we define the period having power transferred as the "active power transfer" period and the period with constant zero power as the "zero power transfer" period.

Following the zoomed window in Fig. 9(a), during active power transfer periods, the inverter output current i_{o12} [supplied to the WPT stage through the compensation inductor L_{f}, cf., (4)] follows the shape of the Rx coil current i_{Rx}, which combines

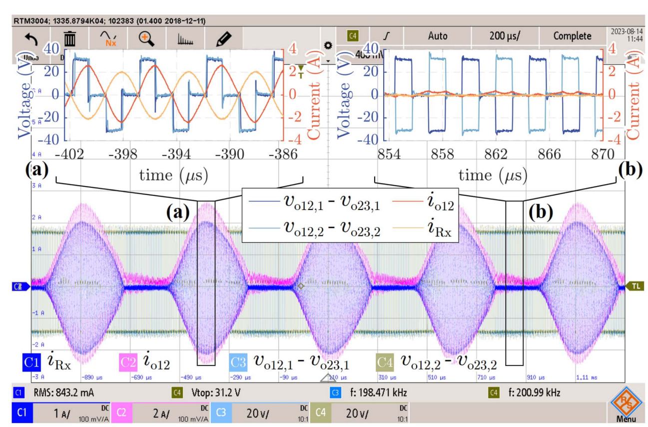

Fig. 9. Waveforms of a noncoherent power combining example at Rx position (2.5,1.5,45°): the inverter output current i_{o12} (Ch2), the ac voltage at frequencies f_1 and f_2 (Ch3, 4), and the Rx coil current i_{Rx} (Ch1). (a) Zoomed version at the active power transfer period. (b) Zoomed version during the zero power transfer period.

both f_1 and f_2 frequencies. The f_1 and f_2 voltage supplies are almost in phase, so it contributes to high instantaneous power transfer to the Rx. In contrast, Fig. 9(b) shows the zero power transfer period, where the currents i_{o12} and i_{Rx} are both zero. The instantaneous power is low because the ac voltage components are nearly out-of-phase. This attribute of the Rx current and inverter current establishes the foundation for efficiency on par with conventional methods, while simultaneously eliminates blind spots.

Next, Fig. 10(a) illustrates coherent power combining waveforms at the example Rx position $(x, y, \theta) = (1.5, 1.5, 45°)$ in Fig. 4(c), where the Rx obtains power from Tx_{11} and Tx_{22}.

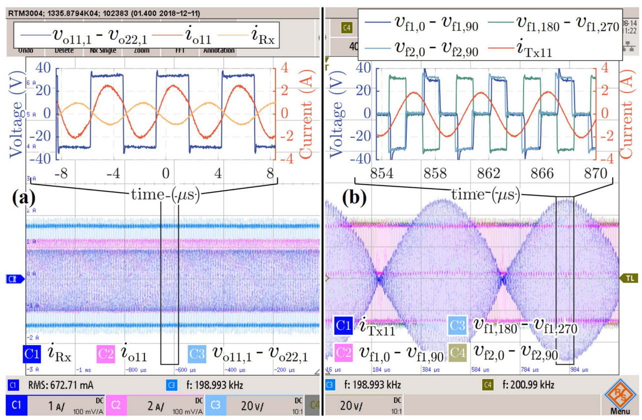

Fig. 10. (a) Waveforms in the coherent power combining special *Case 1* at the same frequency f_1: the Tx and Rx current and voltage and a zoomed window, cf., Rx position (1.5,1.5,45°). (b) Tx-side voltage (Ch2, 3, 4) and current (Ch1) waveforms and a zoomed version.

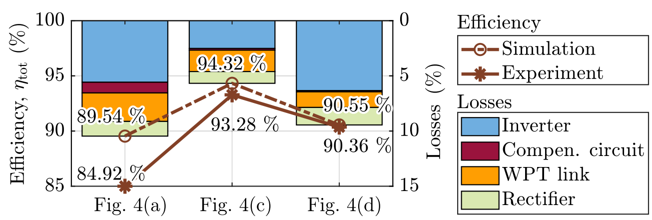

Fig. 11. System efficiency and loss distribution at three example positions in Fig. 4(a) noncoherent: $(2.5, 1.5, 45°)$, Fig. 4(c) coherent *case 1:* $(1.5, 1.5, 45°)$, and Fig. 4(d) coherent *case 2:* $(2.5, 1, 90°)$.

The waveforms do not have any low-frequency envelope since there is only one frequency f_1. The zoomed window of Fig. 10(a) shows the phase relations between the ac supply voltage and the input/output currents. Fig. 10(b) presents all the ac voltage waveforms in the considered Tx area, including $v_{f1,0}$, $v_{f1,90}$, $v_{f1,180}$, $v_{f1,270}$, and $v_{f2,0}$, $v_{f2,90}$. The Tx current i_{Tx11} is also given as an example, validating (5), showing that the Tx current is dependent only on the supply voltage, and thus contains both frequencies, while it is independent of the Rx-side operations.

To evaluate the system performance regarding efficiency and losses in each power stage, Fig. 11 is plotted with both experimental measurements and simulation results. Due to difficulties in measuring ac losses directly in the experiment setup, an *LTspice* model is built based on the used components, showing the same trend of the dc–dc efficiency as in the experimental measurements. Therefore, the losses in each stage can be estimated from simulation results, which are given as bar charts in Fig. 11 referring to the three example Rx positions in Fig. 4. We can notice from Fig. 11 that the coherent *Case 1* has a relatively balanced loss distribution in each power stage, while the inverter loss is still dominant in the noncoherent combining, which could be attributed to switching losses. Detailed investigations of soft-switching operations can be attractive topics for future work. Nevertheless, the principles of noncoherent power combining are successfully verified through the experimental results presented in this section, proving complete elimination of blind spots with the proposed energizing pattern.

V. Conclusion

This article had proposed a novel multi-Tx WPT system based on noncoherent power combining, with predefined Tx currents in terms of their frequencies and phases. With the proper combination of two frequencies and four phases, multi-Tx WPT area energized by the proposed pattern provided Rx full positional and rotational charging freedom. Rx devices could be realized as simple DD or flux-pipe coil structures. A laboratory prototype featuring the proposed large-area Tx energizing pattern was constructed to validate the proposed method. Experimental results demonstrated that the Rx consistently achieves charging efficiency between 82% and 93%, irrespective of its position or orientation. Leveraging the principles of noncoherent power combining, this system effectively eliminated the problem of power transfer blind spots commonly encountered in conventional WPT systems. We concluded that the proposed multi-Tx energizing pattern could serve as modular and scalable building blocks for free-positioning multi-Tx WPT systems.

References

[1] J. Yin, D. Lin, C. K. Lee, T. Parisini, and S. Y. Hui, "Front-end monitoring of multiple loads in wireless power transfer systems without wireless communication systems," *IEEE Trans. Power Electron.*, vol. 31, no. 3, pp. 2510–2517, Mar. 2016.

[2] J. I. Agbinya, "20 Induction Cooking and Heating," in *Wireless Power Transfer 2nd Edition*, Aalborg, Denmark: River Publishers, 2016, pp. 681–702.

[3] S. A. Al Mahmud, I. Panhwar, and P. Jayathurathnage, "Large-area free-positioning wireless power transfer to movable receivers," *IEEE Trans. Ind. Electron.*, vol. 69, no. 12, pp. 12 807–12 816, Dec. 2022.

[4] S. Y. Choi, B. W. Gu, S. Y. Jeong, and C. T. Rim, "Advances in wireless power transfer systems for roadway-powered electric vehicles," *IEEE Trans. Emerg. Sel. Topics Power Electron.*, vol. 3, no. 1, pp. 18–36, Mar. 2015.

[5] T. Feng, Z. Zuo, Y. Sun, X. Dai, X. Wu, and L. Zhu, "A reticulated planar transmitter using a three-dimensional rotating magnetic field for free-positioning omnidirectional wireless power transfer," *IEEE Trans. Power Electron.*, vol. 37, no. 8, pp. 9999–10015, Aug. 2022.

[6] J. Shin et al., "Design and implementation of shaped magnetic-resonance-based wireless power transfer system for roadway-powered moving electric vehicles," *IEEE Trans. Ind. Electron.*, vol. 61, no. 3, pp. 1179–1192, Mar. 2014.

[7] J. M. Miller et al., "Demonstrating dynamic wireless charging of an electric vehicle: The benefit of electrochemical capacitor smoothing," *IEEE Power Electron. Mag.*, vol. 1, no. 1, pp. 12–24, Mar. 2014.

[8] Q. Xu, H. Wang, Z. Gao, Z. Mao, J. He, and M. Sun, "A novel mat-based system for position-varying wireless power transfer to biomedical implants," *IEEE Trans. Magn.*, vol. 49, no. 8, pp. 4774–4779, Aug. 2013.

[9] Z. Zhang and K. T. Chau, "Homogeneous wireless power transfer for move-and-charge," *IEEE Trans. Power Electron.*, vol. 30, no. 11, pp. 6213–6220, Nov. 2015.

[10] F. Lu, H. Zhang, H. Hofmann, and C. C. Mi, "A dynamic charging system with reduced output power pulsation for electric vehicles," *IEEE Trans. Ind. Electron.*, vol. 63, no. 10, pp. 6580–6590, Oct. 2016.

[11] J. Liu, Z. Liu, W. Chen, X. Sun, and H. Su, "An optimized coil array and passivity-based control for receiving side multilevel connected DC-DC converter of dynamic wireless charging," *IEEE Trans. Veh. Technol.*, vol. 71, no. 4, pp. 3715–3726, Apr. 2022.

[12] W. Kim and D. Ahn, "Efficient deactivation of unused LCC inverter for multiple transmitter wireless power transfer," *IET Power Electron.*, vol. 12, no. 1, pp. 72–82, 2019.

[13] S. Li, L. Wang, Y. Guo, C. Tao, and L. Ji, "Power stabilization with double transmitting coils and T-type compensation network for dynamic wireless charging of EV," *IEEE Trans. Emerg. Sel. Topics Power Electron.*, vol. 8, no. 2, pp. 1801–1812, Jun. 2020.

[14] M. Budhia, J. T. Boys, G. A. Covic, and C. Huang, "Development of a single-sided flux magnetic coupler for electric vehicle IPT charging systems," *IEEE Trans. Ind. Electron.*, vol. 60, no. 1, pp. 318–328, Jan. 2013.

[15] M. Budhia, G. A. Covic, J. T. Boys, and C.-Y. Huang, "Development and evaluation of single sided flux couplers for contactless electric vehicle charging," in *Proc. IEEE Energy Convers. Congr. Expo.*, 2011, pp. 614–621.

[16] X. Zhang, Y. Zhang, Z. Zhang, and M. Li, "Mode conversion and structure optimization of quadrature coils for electric vehicles wireless power transfer," *IEEE Trans. Energy Convers.*, vol. 35, no. 2, pp. 575–590, Jun. 2020.

[17] Y. Nagatsuka, N. Ehara, Y. Kaneko, S. Abe, and T. Yasuda, "Compact contactless power transfer system for electric vehicles," in *Proc. Int. Power Electron. Conf.*, 2010, pp. 807–813.

[18] Y. Yao, C. Tang, and Y. Wang, "Crossed flat solenoid coupler for stationary electric vehicle wireless charging featuring high misalignment tolerance," *IET Electr. Power Appl.*, vol. 14, no. 13, pp. 2648–2658, 2020.

[19] X. Li, J. Hu, H. Wang, X. Dai, and Y. Sun, "A new coupling structure and position detection method for segmented control dynamic wireless power transfer systems," *IEEE Trans. Power Electron.*, vol. 35, no. 7, pp. 6741–6745, Jul. 2020.

[20] Y. Li et al., "A new coil structure and its optimization design with constant output voltage and constant output current for electric vehicle dynamic wireless charging," *IEEE Trans. Ind. Informat.*, vol. 15, no. 9, pp. 5244–5256, Sep. 2019.

[21] P. Jayathurathnage, Y. Liu, and J. Kyyrä, "Self-decoupled and integrated coils for modular multitransmitter wireless power transfer systems," *IEEE Trans. Power Electron.*, vol. 37, no. 11, pp. 12 962–12 967, Nov. 2022.

[22] A. Mahesh, B. Chokkalingam, and L. Mihet-Popa, "Inductive wireless power transfer charging for electric vehicles-A review," *IEEE Access*, vol. 9, pp. 137 667–137 713, 2021.

[23] J. H. Kim et al., "Plane-type receiving coil with minimum number of coils for omnidirectional wireless power transfer," *IEEE Trans. Power Electron.*, vol. 35, no. 6, pp. 6165–6174, Jun. 2020.

[24] X. Dai, X. Li, Y. Li, and A. P. Hu, "Maximum efficiency tracking for wireless power transfer systems with dynamic coupling coefficient estimation," *IEEE Trans. Power Electron.*, vol. 33, no. 6, pp. 5005–5015, Jun. 2018.

[25] Y. Yang, J. Wang, Z. Huang, I.-W. Iam, and C.-S. Lam, "Automatic containment of field exposure for roadway wireless electric vehicle charger," *IEEE Trans. Transport. Electrific.*, vol. 9, no. 3, pp. 4121–4131, Sep. 2023.

[26] S. Y. Jeong, J. H. Park, G. P. Hong, and C. T. Rim, "Autotuning control system by variation of self-inductance for dynamic wireless EV charging with small air gap," *IEEE Trans. Power Electron.*, vol. 34, no. 6, pp. 5165–5174, Jun. 2019.

[27] Y. Luo, Y. Song, Z. Wang, R. Mai, B. Yang, and Z. He, "Auto-segment control system with high spatially average power for dynamic inductive power transfer," *IEEE Trans. Transport. Electrific.*, vol. 9, no. 2, pp. 3060–3071, Jun. 2023.

[28] K. Shi, C. Tang, Z. Wang, X. Li, Y. Zhou, and Y. Fei, "A magnetic integrated method suppressing power fluctuation for EV dynamic wireless charging system," *IEEE Trans. Power Electron.*, vol. 37, no. 6, pp. 7493–7503, Jun. 2022.

[29] K. Shi, C. Tang, H. Long, X. Lv, Z. Wang, and X. Li, "Power fluctuation suppression method for EV dynamic wireless charging system based on integrated magnetic coupler," *IEEE Trans. Power Electron.*, vol. 37, no. 1, pp. 1118–1131, Jan. 2022.

[30] Y. Huang, C. Liu, S. Liu, and Y. Xiao, "A selectable regional charging platform for wireless power transfer," in *Proc. 45th Annu. Conf. IEEE Ind. Electron. Soc.*, 2019, pp. 4445–4450.

[31] F. Farajizadeh, D. M. Vilathgamuwa, D. Jovanovic, P. Jayathurathnage, G. Ledwich, and U. Madawala, "Expandable N-legged converter to drive closely spaced multitransmitter wireless power transfer systems for dynamic charging," *IEEE Trans. Power Electron.*, vol. 35, no. 4, pp. 3794–3806, Apr. 2020.

[32] Z. Pantic, S. Bai, and S. M. Lukic, "ZCS $PLX.LCC$-Compensated resonant inverter for inductive-power-transfer application," *IEEE Trans. Ind. Electron.*, vol. 58, no. 8, pp. 3500–3510, Aug. 2011.

[33] Y. Liu, N. Ha-Van, P. Jayathurathnage, J. Kyyrä, and S. A. Tretyakov, "Non-coherent power combining for self-tuning omnidirectional wireless power transfer," in *Proc. 25th Eur. Conf. Power Electron. Appl.*, 2023, pp. 1–8.

[34] X. Lu, P. Wang, D. Niyato, D. I. Kim, and Z. Han, "Wireless charging technologies: Fundamentals, standards, and network applications," *IEEE Commun. Surv. Tuts.*, vol. 18, no. 2, pp. 1413–1452, Apr.–Jun. 2016.

[35] S. Song, Q. Zhang, Z. He, H. Li, and X. Zhang, "Uniform power dynamic wireless charging system with I-type power supply rail and DQ-Phase-Receiver employing receiver-side control," *IEEE Trans. Power Electron.*, vol. 35, no. 10, pp. 11 205–11 212, Oct. 2020.

Yining Liu (Student Member, IEEE) received the B.Sc. and M.Sc. degrees in electrical engineering from the Harbin Institute of Technology, Harbin, China, in 2018 and 2020, respectively. She is currently working toward the doctoral degree in electrical power and energy engineering with the Department of Electrical Engineering and Automation, School of Electrical Engineering, Aalto University, Espoo, Finland.

Her main research interests include wireless power transfer, high-frequency power converters, soft-switching converters, and wide-bandgap devices.

Shamsul Arefeen Al Mahmud received the B.Sc. degree in electrical engineering from United International University, Dhaka, Bangladesh, in 2015, and the M.Sc. degree in autonomous systems from Aalto University, Espoo, Finland, and KTH Royal Institute of Technology, Stockholm, Sweden, in 2020. He is currently working toward the doctoral degree in electrical engineering with the School of Electrical Engineering, Aalto University.

His main research interests include electronics and wireless power transfer.

Nam Ha-Van (Member, IEEE) received the B.Sc. degree in electronics and telecommunications engineering from the School of Electronics and Telecommunications, Hanoi University of Science and Technology, Hanoi, Vietnam, in 2012, and the Ph.D. degree in information and telecommunication engineering from Soongsil University, Seoul, South Korea, in 2019.

From 2019 to 2020, he was a Postdoctoral Researcher with Soongsil University. From 2020 to 2023, he was a Postdoctoral Researcher with the Department of Electronics and Nanoengineering, School of Electrical Engineering, Aalto University, Espoo, Finland, where he is currently a Research Fellow with the Department of Electrical Engineering and Automation. His research interests include wireless power transfer, electromagnetic theory, metamaterials, antennas, and energy harvesting systems.

Prasad Jayathurathnage (Senior Member, IEEE) received the B.Sc. degree in electronics and telecommunications engineering from the University of Moratuwa, Moratuwa, Sri Lanka, in 2009, and the Ph.D. degree in electrical and electronic engineering from Nanyang Technological University, Singapore, in 2017.

From 2017 to 2018, he was a Research Fellow with the Queensland University of Technology, Brisbane, QLD, Australia, and Rolls-Royce-NTU Corporate Lab, Singapore. From 2018 to 2023, he was a Full-Time Postdoctoral Researcher with the School of Electrical Engineering, Aalto University, Espoo, Finland, and an Academic Guest with the Power Electronic Systems Laboratory, ETH Zurich, Zurich, Switzerland. He is currently a Senior Research Engineer with Danfoss Drives, Tampere, Finland, and continues his academic affiliation with Aalto University as an Academic Visitor. He has authored more than 60 research articles in various journals, conferences, and tutorial seminars. His research interests include high-frequency power converters, wide-band-gap devices, passive components, and wireless power transfer.

Dr. Jayathurathnage was the recipient of several accolades for his research, including the Best Paper Awards at IEEE PEMC 2018, IEEE ISMICT 2019, and IEEE SPEC 2022.

Jorma Kyyrä (Member, IEEE) received the M.Sc., Lic.Sc., and D.Sc. degrees in electrical engineering from the Helsinki University of Technology (TKK), which is currently Aalto University, Helsinki, Finland, in 1987, 1991, and 1995, respectively.

Since 1985, he has been with the university in various positions. Since 1996, he has been an Associate Professor of power electronics. Since 1998, he has been a Professor of power electronics. From 2008 to 2009, he was the Dean with the Faculty of Electronics, Communications, and Automation, TKK. From 2009 to 2011, he was the Vice President with Aalto University, Espoo, Finland, where he is currently the Head of the Department of Electrical Engineering and Automation. His research interests include power electronics at large, and the power electronics group with Aalto University has expertise, such as in power electronics for ac drives, dc–dc converters, modeling of converters, filtering of EMI, power factor correction, and distributed power systems.

Sergei A. Tretyakov (Fellow, IEEE) received the Dipl. Engineer-Physicist, Candidate of Sciences (Ph.D.), and D.Sc. degrees in radiophysics from Saint Petersburg State Technical University, Saint Petersburg, Russia, in 1980, 1987, and 1995, respectively.

From 1980 to 2000, he was with the Department of Radiophysics, Saint Petersburg State Technical University. He is currently a Professor of radio science with the Department of Electronics and Nanoengineering, Aalto University, Espoo, Finland. He has authored or coauthored six research monographs and more than 360 journal articles. His current research interests include electromagnetic field theory, complex media electromagnetics, metamaterials, and microwave engineering.

Dr. Tretyakov was the Chairman of the Saint Petersburg IEEE Electron Devices/Microwave Theory and the Techniques/Antennas and Propagation Chapter, from 1995 to 1998, and the General Chair of the International Congress Series on Advanced Electromagnetic Materials in Microwaves and Optics (Metamaterials) and the President of the Virtual Institute for Artificial Electromagnetic Materials and Metamaterials (Metamorphose VI), from 2007 to 2013.